EES Solar

PAPER

View Article Online
View Journal | View Issue

Cite this: *EES Sol.*, 2025, **1**, 881

Photovoltaic properties of BiI_3 with copper interstitials

Rupam Datta,[ab] Kai Trombotto Herfert,[c] Daniel M. Többens,[d] Pirmin Tischler,[b] Martin Peterlechner,[f] Ben Breitung,[g] Marcel Habrik,[ab] Jan Bruder,[ab] Uli Lemmer,[b] Susan Schorr,[de] Alexander Colsmann[ab] and Holger Röhm*[ab]

Received 1st July 2025
Accepted 7th September 2025

DOI: 10.1039/d5el00108k

rsc.li/EESSolar

The synthesis and photovoltaic effect of $Cu_{3x}Bi_{1-x}I_3$ (CBI) thin films were studied. Although CBI was originally inspired by the material class of Caswellsilverites (also known as Rudorffites), an XRD study showed that its crystal structure resembles a BiI_3-cage with interstitial copper. CBI was found to demonstrate optoelectronic properties suitable for solar light harvesting, including a band gap of 1.66 eV and thermal stability up to 333 °C. The corresponding thin film solar cells achieved a peak power conversion efficiency of 0.65%.

Broader Context Statement

This manuscript presents our recent study on the synthesis, characterization, and photovoltaic performance evaluation of $Cu_{3x}Bi_{1-x}I_3$, a novel lead-free, copper-based semiconductor that is closely related to Caswellsilverite (or Rudorffite) metal halides. We report the successful fabrication of $Cu_{3x}Bi_{1-x}I_3$ thin films and highlight their promising optoelectronic properties, including a bandgap of 1.66 eV and excellent thermal stability up to 333 °C. We have integrated these thin films into solar cells, demonstrating a power conversion efficiency of 0.65%. Our findings add to the growing library of lead-free, perovskite-inspired materials and open avenues for further exploration of environmentally benign light-harvesting compounds in photovoltaic applications. We particularly emphasize the structural analysis and discussion of the lattice structure since, during the past couple of months, we noted that a lot of publications in this quickly growing field rather improvidently mislabel novel phases as "perovskites", "rudorffites" or "caswellsilverites". We believe this work will appeal to readers within the fields of optoelectronics, sustainable materials, and photovoltaics, given the pressing need for lead-free and environmentally friendly energy materials.

Introduction

The quest for an eco-friendly energy supply has catalysed significant advancements in photovoltaics. Over the past decade, lead-based organic metal-halide perovskite (OMH) solar cells have gained popularity[1] due to their unique optoelectronic properties and high defect tolerance.[2–4] However, their commercialization is often questioned because of compositional instabilities and potential hazards arising from decomposition products, *i.e.* water-soluble lead salts.[5] Any lead-free surrogate would benefit the environment, enhance the social acceptance of the technology and, not least, simplify the manufacturing process, in particular in compliance with regulatory standards such as the Restriction of Hazardous Substances (RoHS) directive. To date, no straightforward concepts exist to remove the lead from photovoltaic perovskites, which is why the community has set out to explore other "perovskite-inspired" material classes with structural or compositional similarities to OMH perovskites.

Tin (Sn^{2+}) has been investigated as a potential replacement for lead. However, in view of its susceptibility to oxidation from +2 to +4 under ambient conditions, due to the strong shielding effect of the 4d orbital of Sn^{2+}, the stability of the compound remains of concern. The corresponding weaker nuclear attraction of the 5 s lone pairs of electrons fosters recombination losses.[6,7] To date, defect-ordered perovskites and cation-ordered double perovskites such as $Cs_3Sb_2I_9$ and Cs_2AgBiI_6 have been considered promising candidates for lead-free light-harvesting semiconductors.[8] Yet, these materials often suffer from wide band gaps (>2 eV), large exciton binding energies (>100 meV), and low dimensionality. Together, these factors often limit the solar cell power conversion efficiency.[8–11] A closely related perovskite-inspired material class encompasses the all-inorganic Caswellsilverites, named after Caswell Silver, who

[a]*Karlsruhe Institute of Technology (KIT), Material Research Center for Energy Systems, Strasse am Forum 7, 76131 Karlsruhe, Germany. E-mail: holger.roehm@kit.edu*
[b]*Karlsruhe Institute of Technology (KIT), Light Technology Institute, Engesserstrasse 13, 76131 Karlsruhe, Germany*
[c]*Karlsruhe Institute of Technology (KIT), Institute of Applied Material Research – Ceramic Materials and Technologies, Haid-und-Neu Strasse 7, 76131 Karlsruhe, Germany*
[d]*Helmholtz-Zentrum Berlin für Materialien und Energie, Berlin 14109, Germany*
[e]*Institut für Geologische Wissenschaften, Freie Universität Berlin, Berlin 12249, Germany*
[f]*Karlsruhe Institute of Technology (KIT), Laboratory for Electron Microscopy, Engesserstrasse 7, 76131 Karlsruhe, Germany*
[g]*Karlsruhe Institute of Technology (KIT), Institute of Nanotechnology, Hermann-von-Helmholtz-Platz 1, 76344 Eggenstein-Leopoldshafen, Germany*

investigated $NaCrS_2$ in 1982.[12] Later in 2017, Caswellsilverites also became known as Rudorffites, named after Walter Rüdorff, who studied the archetypal $NaVO_2$ in 1954.[13] These compounds exhibit the stoichiometric composition of $A_aB_bX_y$ with $y = a + 3b$, the structure consists of edge-sharing AX_6 and BX_6 octahedra. Caswellsilverites are perovskite-inspired structures having a similar corner-sharing octahedral coordination. The octahedron is a regular geometric shape with the central atom bonded to six atoms at the corners, forming eight faces. Among Caswellsilverites, Ag–Bi–I compounds have been studied extensively (*e.g.*, $AgBiI_4$, Ag_2BiI_5, Ag_3BiI_6, and Ag_2BiI_7).[13] Considering both abundance and cost, replacing Ag with Cu on the A-site appears to be a promising way forward.[14] Yet, synthesizing Caswellsilverites with a high Cu : Bi ratio (>1) remains challenging,[15] and thus, only limited structural information for higher Cu : Bi ratios (>1) has been reported to date. Previous literature on Cu-substitution in Caswellsilverites primarily reports $CuBiI_4$ with a Cu : Bi ratio of 1 : 1.[16] It was reported that higher Cu-content in a precursor solution can leverage the formation of Caswellsilverites with the chemical formula $Cu_iBi_jI_m$ where, i and j are molar concentrations of Cu and Bi respectively and $m = i + 3j$. For instance, $i = 3$ and $j = 1$ can yield a Caswellsilverite Cu_3BiI_6.[17] This may not always be true as some compounds that fit the stoichiometry of $A_aB_bX_{a+3b}$ lack octahedral coordination, which is essential to qualify as Caswellsilverites.

In this work, the challenge of identifying lead-free photovoltaic absorbers is addressed by investigating copper-rich bismuth iodides with compositions beyond the conventional Caswellsilverite range. Motivated by the structural limitations of existing Cu–Bi–I compounds and the scarcity of data on phases with high copper content, $Cu_{3x}Bi_{1-x}I_3$ thin films and powders are synthesized from a precursor solution with a 3 : 1 Cu : Bi molar ratio. Although the apparent stoichiometry fits the Caswellsilverite-type $A_aB_bX_y$ formula ($y = a + 3b$), the structure deviates from classical octahedral coordination. In the following sections, the synthesis strategy, structural features, optoelectronic properties, and solar cell integration of this material are presented, and its potential for environmentally benign photovoltaic applications is evaluated.

Results and discussion

To determine the crystalline phase present in $Cu_{3x}Bi_{1-x}I_3$, powder X-ray diffraction (PXRD) measurements were conducted. The Rietveld refined diffractogram from a Bragg–Brentano geometry is shown in Fig. 1a, using Cu Kα radiation over a 2θ range from 5° to 100°.

The diffraction pattern reveals a multi-phase composition. The predominant phase, accounting for 56(1) wt%, was identified as α-CuI (ICSD 33727)[18] with characteristic sharp reflections along the <111> directions and broadened features along <100>.

Another significant phase, constituting 35(1) wt%, corresponded to a previously unreported rhombohedral $Cu_{3x}Bi_{1-x}I_3$ phase, derived from Cu-interstitial incorporated BiI_3 structure (ICSD 26083).[19] The space group was identified as $R\bar{3}$ (trigonal), and the structural file can be found in the SI. This phase

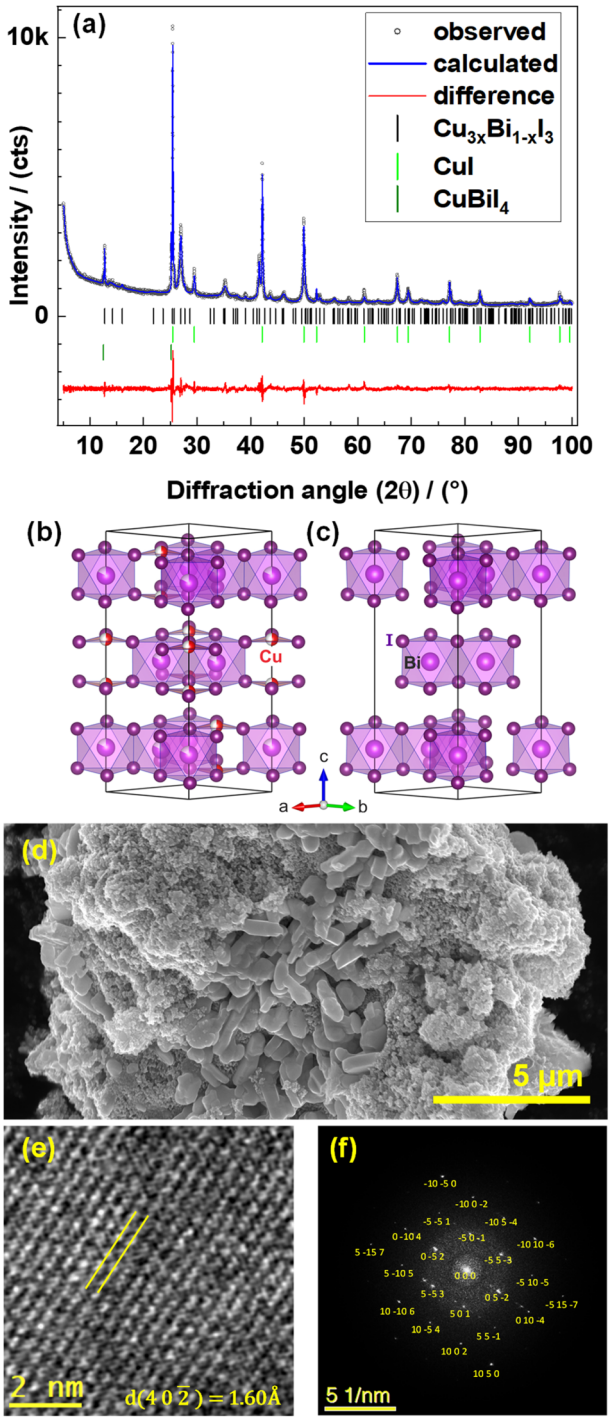

Fig. 1 (a) Rietveld refinement of the PXRD data. For $CuBiI_4$ only the observed peaks were included; (b) structure of the new rhombohedral $Cu_{3x}Bi_{1-x}I_3$ phase with Cu in trifold planar coordination, and (c) the structure of BiI_3 for comparison; (d) the SEM micrograph of the powder sample shows μm-sized $Cu_{3x}Bi_{1-x}I_3$ micro/nanorods (center). Smaller crystalline grains are visible towards the edge of the particle (Fig. S1, SI); (e) HRTEM of $Cu_{3x}Bi_{1-x}I_3$ showing d-spacing for (40$\bar{2}$), and (f) indexed SAED spots of the same domain.

crystallized in a layered structure and exhibited strong anisotropic broadening of the 00l reflections, indicating stacking fault disorder rather than limited crystallite size. This layered

structure is similar to the structure of BiI_3, which is 2-dimensional and consists of sheets of edge-sharing BiI_6-octahedra. Note, that in BiI_3 some of the octahedra in the layers are empty (I_6-octahedra with indicating a vacancy). The refined unit cell parameters are $a = 7.5171(2)$ Å, $c = 20.7458(10)$ Å, with interstitial Cu within the BiI_6 octahedra layers. The interstitial Cu atoms are in a 3-fold planar coordination by I, which is unusual. Attempts to place Cu either in an octahedral coordination as expected in the Caswellsilverite-type structure or in a tetrahedral coordination found in $Bi_{1.5}Cu_{1.44}$ I_6 (ICSD 114003)[15] resulted in an occupation factor refining to very low or negative values. This is where the structure distinguishes from the Caswellsilverite-type. In the case of $Cu_{3x}Bi_{1-x}I_3$, Cu does not coordinate in tetrahedra or octahedra with I, but our results indicate a 3-fold-planar coordination. That is, each Cu atom is bonded to three I atoms within the same plane, forming a triangle around the Cu atom. The correct position of the Cu atoms was determined from difference-Fourier maps based on the BiI_3 structure.

The refined structure of $Cu_{3x}Bi_{1-x}I_3$ phase (Fig. 1b) showed that the interstitial Cu^+ occupied the trigonal faces of those octahedra of BiI_3 layers (Fig. 1c) that are empty. A detailed discussion of the structure, including a comparison with similar structures and Caswellsilverite, can be found in the SI (Fig. S2a and S2b). The final refinement yielded satisfactory residuals (Weighted R-factor (R_{wp}) = 5.8%, expected R-factor ($R_{expected}$) = 3.6%, goodness-of-fit indicator $\chi^2 = 2.7$); however, anisotropic peak broadening posed modelling challenges, especially for the rhombohedral phase.

To assess the crystallinity of grains, Scanning Electron Microscopy (SEM; Fig. 1d) and high-resolution Transmission Electron Microscopy (HRTEM; Fig. 1e–f) analyses were performed. SEM further confirmed that the single-crystalline $Cu_{3x}Bi_{1-x}I_3$ micro-rods had grown along a single axis in a layered structure. Zooming in on the outer area also confirmed the formation of crystalline nano-rod structures (Fig. S1). Using a Gatan digital microscope to process and analyse HRTEM images, high crystallinity was observed in those $Cu_{3x}Bi_{1-x}I_3$ micro/nano-rods (Fig. 1e). The selected area electron diffraction (SAED) pattern in Fig. 1f, indexed (using CrysTBox cell viewer)[20] along the $\langle\bar{1}25\rangle$ zone axis, confirmed the high crystallinity of the $Cu_{3x}Bi_{1-x}I_3$ phase at the local scale. Sharp and well-defined diffraction spots were observed, consistent with a rhombohedral structure and without significant diffuse scattering or streaking, indicating minimal stacking disorder in this region. The visibility of multiple higher-order reflections further supports the absence of significant dynamic scattering or amorphous contributions. Although HRTEM and SAED confirm that individual $Cu_{3x}Bi_{1-x}I_3$ micro/nano-rods are locally well-ordered and highly crystalline, the powder XRD data reveal anisotropic broadening of the $00l$ reflections, consistent with stacking fault disorder along the crystallographic $\vec{c}$-axis. This suggested that while individual domains exhibited locally perfect order, the long-range stacking of layers across domains was disrupted – a characteristic frequently observed in layered intercalated compounds and van der Waals solids.[21–23] From the Rietveld refinement of XRD data, atomic occupancies were refined to maintain overall charge neutrality, resulting in a composition of $Cu_{0.72}Bi_{0.76}I_3$, where $x = 0.24$ as average composition of the phase. From SAED refinement using CrysTBox, the value of $x = 0.16$ was identified, and hence, the composition is $Cu_{0.48}Bi_{0.84}I_3$, which is a local composition determined for a certain grain. The detailed SAED analysis report is presented in Table S1 and Fig. S3. Furthermore, using Transmission Electron Microscopy (TEM) and Energy-Dispersive X-ray Spectroscopy (EDX) on a representative sample at a random position within the compound confirmed the presence of elemental distribution within the grains (Fig. S4).

Following the structural investigation, the material properties of $Cu_{3x}Bi_{1-x}I_3$, which are crucial for its application in solar cells, were examined. Any (novel) light-harvesting semiconductor must exhibit a minimum thermal stability against decomposition to withstand the conditions in various climates and under solar illumination. The thermal stability of $Cu_{3x}Bi_{1-x}I_3$ was investigated by conducting combined Thermogravimetric Analysis (TGA) and Differential Thermal Analysis (DTA) of the as-synthesized $Cu_{3x}Bi_{1-x}I_3$ powder, from room temperature up to 900 °C crossing multiple decomposition thresholds (Fig. 2a). $Cu_{3x}Bi_{1-x}I_3$ is thermally stable up to 333 °C. Towards 440 °C, a mass loss of 42.5% can be seen. Another mass loss of 56% is visible between 580 °C and 790 °C. The initial slope of mass loss at 440 °C was attributed to the decomposition of BiI_3, resulting in the release of I_2. The mass loss of I_2 released from BiI_3 is 43% (*i.e.,* 253.80 g mol^{-1}: 589.68 g mol^{-1}), which is very close to the experimental finding. Likewise, the second slope of mass loss between 580 °C and 790 °C may indicate the decomposition of CuI, as a trace amount of copper was found in

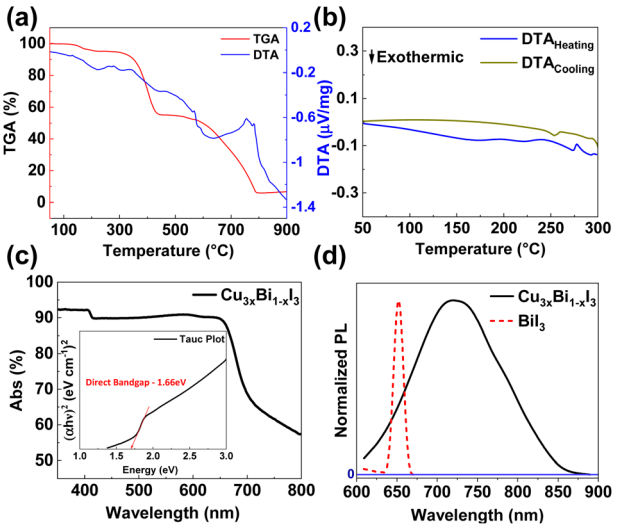

Fig. 2 (a) TGA (red) and DTA (blue) of $Cu_{3x}Bi_{1-x}I_3$ during heating of the sample up to 900 °C. (b) More detailed DTA during heating (blue) and cooling (green) from 50 °C to 300 °C. The peaks at 260 °C (cooling) and 277 °C (heating) can be attributed to a phase change. (c) Absorption spectrum of $Cu_{3x}Bi_{1-x}I_3$. Inset: the Tauc plot of the absorption shows the direct band gap E_g = 1.66 eV. (d) Photoluminescence spectrum of $Cu_{3x}Bi_{1-x}I_3$ with reference to the absorption of BiI_3 at room temperature.

the crucible after the measurement was completed. While the TGA analysis shows only minimal mass loss below 333 °C, indicating that $Cu_{3x}Bi_{1-x}I_3$ appears to be stable, some minor DTA features were observed within this stable temperature regime, prompting us to investigate this regime more closely. The more detailed DTA analysis in Fig. 2b reveals endothermic and exothermic peaks at 277 °C and 260 °C, respectively, during heating and cooling. Since both peaks are very close, this likely indicates a phase transition.

For the efficient harvesting of sunlight in photovoltaic devices, a semiconductor band gap close to 1.3 eV is considered ideal. This value maximizes absorption of the solar spectrum while minimizing thermalization losses.[24] The absorption spectrum of a representative spin-coated $Cu_{3x}Bi_{1-x}I_3$ thin film is depicted in Fig. 2c. Primary absorption onset was observed at 715 nm, corresponding to a band gap energy of 1.73 eV. Another minor absorption edge was observed at 430 nm, attributed to defect states that may originate from vacancies or interstitials in the crystal lattice.[25] A direct band gap of 1.66 eV was derived from the Tauc plot of the absorption, depicted in the inset of Fig. 2c. Although PXRD analysis shows α-CuI as the majority crystalline phase (56 wt%), the optoelectronic and EQE measurements confirm that the photovoltaic response arises primarily from the $Cu_{3x}Bi_{1-x}I_3$ phase (35 wt%). The absorption onset at 715 nm and the direct bandgap of 1.66 eV (Fig. 2c) are inconsistent with α-CuI, which has a wide bandgap (3.0 eV) and absorbs only in the UV. Fig. 2d shows the room temperature photoluminescence (PL) of the $Cu_{3x}Bi_{1-x}I_3$ film with a peak wavelength of $\lambda_{PL} = 725$ nm. For reference, the dashed red line shows the photoluminescence (PL) peak of a neat BiI_3 sample at 650 nm. The difference suggests that the interstitial copper has a significant impact on the optoelectronic properties of the BiI_3 cage. This substantial PL redshift in $Cu_{3x}Bi_{1-x}I_3$ indicates a modification of the band-edge electronic structure due to interstitial Cu^+ incorporation. This shows no correspondence with known α-CuI emission, which is typically weak or absent in the visible range. These Cu^+ ions, coordinated in an atypical trigonal planar geometry within the BiI_3 framework, introduce local lattice distortions and electronic perturbations that give rise to band tailing and shallow defect states.[26] This results in radiative recombination from energetically lower-lying states, consistent with the observed PL redshift. Additionally, the presence of a secondary absorption edge near 430 nm is attributed to sub-bandgap transitions involving Cu-induced shallow traps, further confirming the electronic impact of interstitial Cu in this structure.[27] Despite its structural presence, α-CuI plays no major role in optical absorption and charge generation under device operation conditions. The dominant contribution to photovoltaic performance can therefore be attributed to the interstitially modified $Cu_{3x}Bi_{1-x}I_3$ phase. We note that so far, we were not able to synthesize thin films without the photovoltaically "passive" α-CuI phase, either by changing stoichiometry of the precursor or by varying annealing temperatures. At this point it is yet uncertain whether this phase is required as a matrix for the formation of the $Cu_{3x}Bi_{1-x}I_3$ thin film and whether α-CuI is detrimental to the device performance. This supports the conclusion that a new compound has formed and that the observations do not originate from a mere mixture of the precursors CuI and BiI_3. We note that the Raman spectra of $Cu_{3x}Bi_{1-x}I_3$ thin films on glass also did not match those of the precursors (Fig. S5). The PL peak at 725 nm observed at room temperature is slightly redshifted compared to the absorption of $Cu_{3x}Bi_{1-x}I_3$, which may originate from a lattice expansion or electron–phonon interaction due to the localized thermal input by the laser beam used for excitation.[28]

Lastly, the ionization potential IP = 5.29 eV was derived from photo-electron spectroscopy yield in air (PESA) measurements on $Cu_{3x}Bi_{1-x}I_3$ thin films. An electron affinity (EA) of 3.55 eV was estimated by subtracting the band gap energy from the IP. Further details on the PESA measurements are provided in Fig. S6.

After investigation of the fundamental properties of $Cu_{3x}Bi_{1-x}I_3$, we optimized the thin films for integration into solar cells. Different substrate surfaces can influence the growth of subsequent layers during deposition. Therefore, we examined $Cu_{3x}Bi_{1-x}I_3$ deposition on several hole transport layers (HTLs) and interface modifiers to assess film quality and morphology, namely poly(3,4-ethylene dioxythiophene): poly(styrene sulfonate) (PEDOT:PSS), [2-(3, 6-dimethoxy-9H-carbazol-9-yl) ethyl] phosphonic acid (MeO-2PACz), poly[bis(4-phenyl)(2,4,6-trimethylphenyl)amine] (PTAA) as well as a combination of MeO-2PACz and PTAA. All of these HTLs are established in thin film solar cell applications and energetically match with the hole-transport energy, *i.e.* the IP, of $Cu_{3x}Bi_{1-x}I_3$. The HTLs were deposited atop a pre-structured indium tin oxide electrode on glass. After subsequent deposition of the $Cu_{3x}Bi_{1-x}I_3$ film, the samples were annealed at 60 °C. Further details on the influence of the annealing temperature on the film formation can be found in Fig. S7. Fig. S7 reveals that at elevated temperatures (≥120 °C), the $Cu_{3x}Bi_{1-x}I_3$ films exhibit the formation of discrete islets on the substrate surface. This phenomenon is attributed to thermally driven recrystallization and enhanced surface rearrangement within the film, which can promote phase segregation or dewetting, particularly in thin films with incomplete nucleation coverage. Such morphological evolution at higher temperatures may compromise film continuity and interfacial contact, thereby limiting efficient charge extraction in photovoltaic devices. To monitor the thin film quality of $Cu_{3x}Bi_{1-x}I_3$ atop either of the HTLs, Atomic Force Microscopy (AFM) was performed on all samples, as shown in Fig. 3. $Cu_{3x}Bi_{1-x}I_3$ coated on PEDOT:PSS (Fig. 3a) shows a non-homogeneously covered surface and the formation of islets. Likewise, $Cu_{3x}Bi_{1-x}I_3$ forms patches on top of MeO-2PaCz (Fig. 3b) and PTAA (Fig. 3c), which we attribute to the hydrophobic surfaces formed by these two HTLs. We note that no differences were observed in wetting with or without ozone plasma treatment of the ITO electrodes, as the $Cu_{3x}Bi_{1-x}I_3$ layer is not in direct contact with the ITO but with the respective HTLs. Yet, thin films with lower surface roughness atop a combination of MeO-2PACz and PTAA were achieved (Fig. 3d). The bottom right area of the image still shows thickness variations of the film that occasionally occurred in the outer regions of the substrate that we used for parameter optimization, and likely stem from drying artefacts after spin coating.

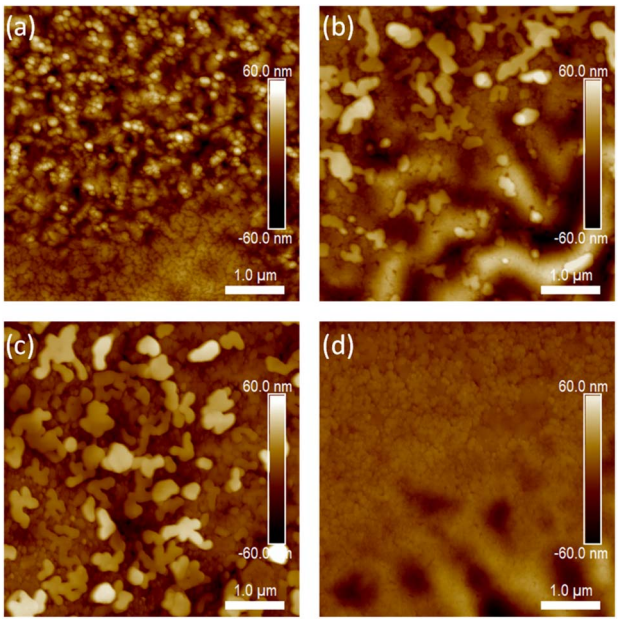

Fig. 3 Atomic Force Micrographs show the topography of $Cu_{3x}Bi_{1-x}I_3$ deposited on (a) PEDOT:PSS, (b) MeO-2PACz, (c) PTAA and (d) PTAA on top of MeO-2PACz. The overall film homogeneity is satisfactory atop PEDOT:PSS and rather poor atop either Meo-2PACz or PTAA due to wetting issues. The film roughness and resulting device performance was maximized using a bilayer of PTAA and MeO-2PACz (d).

Nevertheless, the inner regions of the substrate that contain the photoactive area of the solar cell are fully covered. Table S2 summarizes the root mean square (RMS) roughness of $Cu_{3x}Bi_{1-x}I_3$ on top of each HTL, suggesting the surface roughness is lowest for PTAA on top of MeO-2PACz amongst all four versions.

To evaluate their photovoltaic performance, the $Cu_{3x}Bi_{1-x}I_3$ thin films were incorporated into solar cells with the device architecture depicted in Fig. 4a, inspired by typical inverted lead-halide perovskite solar cells. Fig. 4b summarizes the transport energies of semiconductors and electrodes. Fig. 4c shows the *J–V* curves of representative solar cells in the dark and under illumination (1 sun, ASTM1.5 g). Under illumination, the $Cu_{3x}Bi_{1-x}I_3$ solar cells exhibited an average power conversion efficiency (PCE) of 0.47%. The champion device exhibited a PCE = 0.65%. The average open-circuit voltage of 14 solar cells was $V_{OC} = 0.53 \pm 0.10$ V. Additionally, the short-circuit current $J_{SC} = 2.54$ mA cm^{-2} of the champion device matched the integrated photocurrent of the typical external quantum efficiency (EQE, Fig. 4d) of the same device, which is $J_{EQE} = 2.41$ mA cm^{-2}. The edge of the EQE around 725 nm matches the peak position of the PL of $Cu_{3x}Bi_{1-x}I_3$ (Fig. 2d). This EQE contribution is well beyond the PL peak wavelength of pure BiI_3 (650 nm), which again validates the photovoltaic activity of $Cu_{3x}Bi_{1-x}I_3$. The average J_{SC} was 2.46 ± 0.08 mA cm^{-2}. Forward and reverse *J–V* scans (Fig. 4c) reveal negligible hysteresis, with nearly identical PCE, V_{OC}, and J_{SC} values obtained in both sweep directions. This indicates that ion migration or interfacial charging effects are minimal under the present device configuration. The flat saturation dark currents in the reverse direction indicate a homogeneous and shunt-free light-harvesting layer. Under illumination, the slope of the *J–V* curve in the reverse direction and the fill factor FF = 34 ± 7% suggest strong bimolecular recombination. The relatively modest fill factor and short-circuit current observed in $Cu_{3x}Bi_{1-x}I_3$ solar cells are likely influenced by non-radiative recombination pathways at grain interfaces and imperfect contact at heterojunctions. As shown in Fig. 3, the surface coverage and uniformity of the $Cu_{3x}Bi_{1-x}I_3$ absorber layer are strongly dependent on the underlying hole transport layer (HTL). Deposition onto hydrophobic HTLs such as MeO-2PACz and PTAA results in film textures characterized by isolated domains and incomplete substrate coverage. This behaviour is further accentuated at elevated annealing temperatures, where the formation of discrete crystalline islets becomes more pronounced (Fig. S7), likely due to enhanced recrystallization and solvent redistribution during drying. Conversely, deposition on a bilayer of PTAA atop MeO-2PACz promotes more uniform film formation with reduced surface roughness, which correlates with improved device metrics. These findings underscore the importance of interface energetics and surface chemistry in controlling thin film growth and charge transport across the heterojunction.

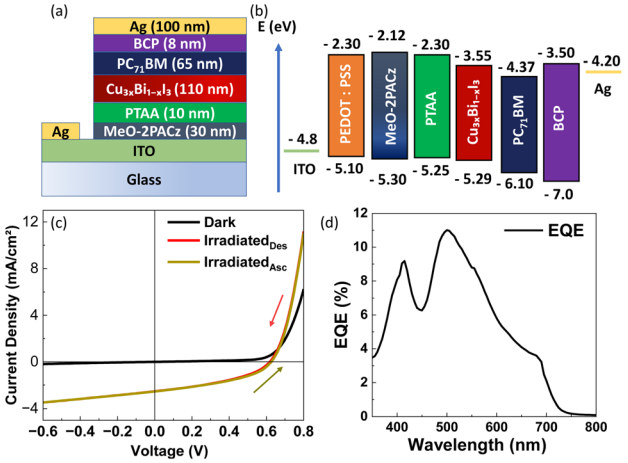

Fig. 4 (a) Architecture of the $Cu_{3x}Bi_{1-x}I_3$ solar cells. (b) Relevant charge carrier transport energies of the individual layers from the architecture (and also of PEDOT:PSS). (c) *J–V* curve of the champion solar cell in the dark and under illumination, measured in forward and reverse directions. (d) The External Quantum Efficiency (EQE) shows photocurrent generation up to 740 nm matching the optical band gap of $Cu_{3x}Bi_{1-x}I_3$.

Conclusion

$Cu_{3x}Bi_{1-x}I_3$ powder and thin films were synthesized in a Cu-rich solution using a Cu : Bi ratio of 3 : 1. While this phase could easily be mistaken for a Caswellsilverite, it was found that Cu rather forms interstitials within the BiI_3 structure. The corresponding solar cells yielded a maximum PCE of 0.65%. Thus, $Cu_{3x}Bi_{1-x}I_3$ introduces a novel compound to the class of Cu/Ag/Bi-based photovoltaic materials, the growing library of perovskite-inspired materials, and the quest for eco-friendly light-harvesting layers. In particular, the band gap of 1.66 eV, which is very close to the Shockley–Queisser optimum, is very

promising. Further compositional optimization of $Cu_{3x}Bi_{1-x}I_3$ will likely enhance the device performances in produced thin films even more by maximizing phase purity and by decreasing the defect density. Future work should also focus on systematic interfacial engineering and HTL surface modification to further improve thin film homogeneity, suppress interfacial recombination to unlock the full photovoltaic potential of $Cu_{3x}Bi_{1-x}I_3$ light absorbing layers. The selection of layer architectures should also consider long-term stability in fully integrated solar cell devices and device fabrication on larger areas.

Author contributions

R. D., A. C., and H. R. designed the study and directed the work. R. D. designed and conducted all the experimental work. R. D., and K. T. H. conducted SEM, and TGA procedures and measurements. S. S., and D. M. T. performed the analysis of the XRD pattern and refined the structure. P. T. assisted with the Raman mapping procedure and measurements. M. P. assisted with the HR-TEM and EDX measurements. M. H. assisted with the EQE measurement. J. B. took the AFM images. R. D. performed the detailed analysis and interpretations of HR-TEM images, SAED patterns, PL and AFM images.

Conflicts of interest

There are no conflicts to declare.

Data availability

Other raw measurement data used in this manuscript is available upon request.

CCDC 2467353 contains the supplementary crystallographic data for this paper.[29]

The data supporting this article have been included as part of the SI. Supplementary information: A detailed description on experimental process, and characterization. See DOI: **https://doi.org/10.1039/d5el00108k**.

Acknowledgements

All authors acknowledge funding by the Carl-Zeiss Foundation under the project "KeraSolar". H. R. and A. C. also acknowledge support by the Helmholtz Association (38.01.02) under the research program "Materials and Technologies for the Energy Transition" (MTET). H. R. and R. D. gratefully acknowledge funding by the Vector Foundation (project MolKristall).

Notes and references

1 A. Kojima, K. Teshima, Y. Shirai and T. Miyasaka, *J. Am. Chem. Soc.*, 2009, **131**, 6050–6051.
2 A. K. Jena, A. Kulkarni and T. Miyasaka, *Chem. Rev.*, 2019, **119**, 3036–3103.
3 W.-J. Yin, T. Shi and Y. Yan, *Appl. Phys. Lett.*, 2014, **104**, 063903.
4 J. Y. Kim, J.-W. Lee, H. S. Jung, H. Shin and N.-G. Park, *Chem. Rev.*, 2020, **120**, 7867–7918.
5 M. Lyu, J. H. Yun, P. Chen, M. Hao and L. Wang, *Adv. Energy Mater.*, 2017, **7**, 1602512.
6 M.-G. Ju, J. Dai, L. Ma and X. C. Zeng, *J. Am. Chem. Soc.*, 2017, **139**, 8038–8043.
7 M. Zhang, Z. Zhang, H. Cao, T. Zhang, H. Yu, J. Du, Y. Shen, X.-L. Zhang, J. Zhu and P. Chen, *Mater. Today Energy*, 2022, **23**, 100891.
8 A. Chakraborty, N. Pai, J. Zhao, B. R. Tuttle, A. N. Simonov and V. Pecunia, *Adv. Funct. Mater.*, 2022, **32**, 2203300.
9 Z. Jin, Z. Zhang, J. Xiu, H. Song, T. Gatti and Z. He, *J. Mater. Chem. A*, 2020, **8**, 16166–16188.
10 Y. Lei, S. Wang, J. Xing, H. Xu, J. Han and W. Liu, *Inorg. Chem.*, 2020, **59**, 4349–4356.
11 Y. Tang, M. Liang, B. Chang, H. Sun, K. Zheng, T. Pullerits and Q. Chi, *J. Mater. Chem. C*, 2019, **7**, 3369–3374.
12 A. Okada and K. Keil, *Am. Mineral.*, 1982, **67**, 132–136.
13 I. Turkevych, S. Kazaoui, E. Ito, T. Urano, K. Yamada, H. Tomiyasu, H. Yamagishi, M. Kondo and S. Aramaki, *ChemSusChem*, 2017, **10**, 3754–3759.
14 B. Zhang, Y. Lei, R. Qi, H. Yu, X. Yang, T. Cai and Z. Zheng, *Sci. China Mater.*, 2019, **62**, 519–526.
15 H. C. Sansom, L. R. Buizza, M. Zanella, J. T. Gibbon, M. J. Pitcher, M. S. Dyer, T. D. Manning, V. R. Dhanak, L. M. Herz and H. J. Snaith, *Inorg. Chem.*, 2021, **60**, 18154–18167.
16 P. Fourcroy, D. Carre, F. Thevet and J. Rivet, *Acta Crystallogr. Sect. C Cryst. Struct. Commun.*, 1991, **47**, 2023–2025.
17 A. K. Baranwal, H. Masutani, H. Sugita, H. Kanda, S. Kanaya, N. Shibayama, Y. Sanehira, M. Ikegami, Y. Numata and K. Yamada, *Nano Convergence*, 2017, **4**, 1–14.
18 Y. Yude, H. Boysen and H. Schulz, *Z. Kristallogr.*, 1990, **191**, 79–91.
19 J. Trotter and T. Zobel, *Z. Kristallogr.*, 1966, **123**, 67.
20 M. Klinger and A. Jager, *J. Appl. Crystallogr.*, 2015, **48**, 2012–2018.
21 S. Hull and D. Keen, *Phys. Rev. B: Condens. Matter Mater. Phys.*, 1994, **50**, 5868.
22 R. Batchelor and T. Birchall, *Struct. Sci.*, 1982, **38**, 1260–1263.
23 a. G. Wiegers, *Prog. Solid State Chem.*, 1996, **24**, 1–139.
24 S. Rühle, *Solar energy*, 2016, **130**, 139–147.
25 A. Janotti and C. G. Van de Walle, *J. Cryst. Growth*, 2006, **287**, 58–65.
26 Y. Zhao, M. Tripathi, K. Čerņevičs, A. Avsar, H. G. Ji, J. F. Gonzalez Marin, C.-Y. Cheon, Z. Wang, O. V. Yazyev and A. Kis, *Nat. Commun.*, 2023, **14**, 44.
27 K. Alshehri and I. J. Thin, *Fil. Sci. Tec.*, 2024, **13**, 235–247.
28 K. Wei, Z. Xu, R. Chen, X. Zheng, X. Cheng and T. Jiang, *Opt. Lett.*, 2016, **41**, 3821–3824.
29 R. Datta, K. Herfert, D. Többens, P. Tischler, M. Peterlechner, B. Breitung, M. Habrik, J. Bruder, U. Lemmer, S. Schorr, A. Colsmann and H. Röhm, CCDC 2467353: Experimental Crystal Structure Determination, 2025, DOI: **10.5517/ccdc.csd.cc2nth11**.